J. Phys. B: At. Mol. Phys. **17** (1984) 1405–1425. Printed in Great Britain

Single ionisation of multiply charged xenon ions by electron impact

C Achenbach†, A Müller†, E Salzborn† and R Becker‡

† Institut für Kernphysik, Universität Giessen, D-6300 Giessen, West Germany
‡ Institut für Angewandte Physik, Universität Frankfurt, D-6000 Frankfurt, West Germany

Received 8 September 1983, in final form 2 December 1983

Abstract. Single-ionisation cross sections $\sigma_{q,q+1}$ for electrons incident on Xe^{q+} ions ($q = 1$, 2, 3, 4) have been measured for electron energies up to 700 eV by employing a crossed beams technique. The results for Xe^{3+} ions agree with previous experimental data of Gregory *et al.* The obtained cross sections increasingly exceed distorted wave with exchange (DWX) calculations of Younger for direct ionisation by factors of up to about five when the charge state of the parent ions is increased from $q = 1$ to $q = 4$. The cross sections $\sigma_{3,4}$ and $\sigma_{4,5}$ show an unexpected enhancement at electron energies around 100 eV. These features are attributed to indirect ionisation processes, which probably also cause another unusual result: for the first time we found a case where ionisation of an atomic ion becomes easier when its charge state is increased; namely for electron energies above 250 eV $\sigma_{4,5}$ is greater than $\sigma_{3,4}$.

1. Introduction

Electron impact ionisation of atoms and ions is one of the fundamental collision processes in all types of plasmas—in astrophysical objects as well as in laboratory discharges. Many of the plasma properties depend on the state of ionisation of ions in these plasmas. Cross section data are needed for plasma modelling; however, both experimental and theoretical knowledge, especially about ionisation of multiply charged ions, is still rather limited.

Quantum theoretical calculations of cross sections for electron impact single ionisation have been carried out in Coulomb–Born (Golden and Sampson 1977, 1978, 1980, Rudge and Schwartz 1966, Moores and Nussbaumer 1969, Moores 1978) and distorted-wave approximations (Younger 1981, 1982a, b) and agree with the experiments as long as direct ejection of individual electrons from the ion prevails. However, previous measurements (Peart and Dolder 1975, Crandall *et al* 1979, Falk *et al* 1981) showed that indirect ionisation mechanisms may dominate the direct process.

(i) Excitation of an electron from an inner shell to a discrete bound state followed by autoionisation.

(ii) Formation of a highly excited resonance state by dielectronic recombination followed by double Auger autoionisation (LaGattuta and Hahn 1981, Henry and Msezane 1982).

Combined theoretical and experimental efforts have gained some insight into the relative contributions of direct and indirect processes contributing to single ionisation (Bottcher *et al* 1983, Gregory *et al* 1983, Falk *et al* 1983, Gregory and Crandall

1983, Pindzola *et al* 1983), however, agreement of calculated and measured cross sections is still elusive (Crandall 1982a). Further measurements on multiply charged ions are needed as a basis for the development of reliable theoretical concepts to reach a detailed understanding of electron impact ionisation.

Our present measurement extends previous crossed beams experiments on electron impact ionisation of multiply charged Ar^{q+} ions ($q = 1, \ldots, 5$) (Müller *et al* 1980) to the investigation of more complex ions Xe^{q+} ($q = 1, 2, 3, 4$). Our results are partly complementary to recent measurements by Gregory *et al* (1983).

We have improved our experimental technique by simultaneous measurement of parent and product ions and by more accurate determination of the background signals mainly due to stripping collisions in the residual gas. The operating electron gun was moved out of the ion-beam line instead of switching off the electron beam. Thus, the relative uncertainties of the present cross section measurements could be considerably reduced.

2. Apparatus

2.1. General

Figure 1 shows a schematic view of the apparatus. The present arrangement is similar to that used by Müller *et al* (1980). In an electron-beam ion source multiply charged

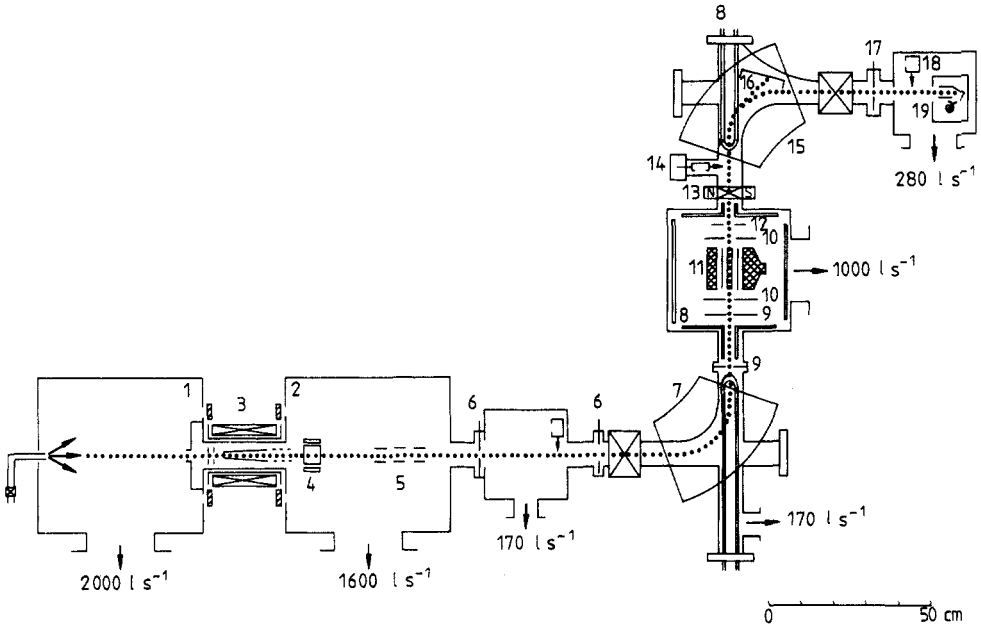

Figure 1. Schematic view of the total experimental arrangement: 1, vacuum tank with gas feed system; 2, vacuum tank with deflecting steerer plates (4) and einzel lens (5); 3, electron-beam ion source; 6, iris apertures; 7, 15, analysing magnets; 8, liquid-N_2-cooled copper plates; 9, ion-beam collimating apertures; 10, shielding plates; 11, electron gun; 12, 17, iris apertures; 13, steering magnet; 14, 18, movable Faraday cups; 16, Faraday cup; 19, single-particle detector.

xenon ions are produced from neutral Xe gas by typically 4 keV electron impact. The ions are continuously extracted and accelerated to ground potential by a voltage of 10 kV. Two pairs of electric field plates and an einzel lens are used to steer and focus the ion beam. A 90° double focusing magnet (7) separates the ions into beams of given charge and mass. The desired ion beam is passed through two collimating apertures (9) and intersects an intense ribbon-shaped electron beam at an angle of 90°. Some of the ions are further ionised by electron impact. By a second double focusing 90° analysing magnet the ionised ions are separated from the parent ion beam and are directed into a single-particle detector (19). The current of the parent ions is measured by a Faraday cup (16) with an effective surface of $2\times25\,\mathrm{cm}^2$ installed inside the magnet chamber (15). Two iris apertures (12, 17) serve to control the ion-beam diameter during the measurements. The Faraday cups (14, 18) can be moved into the beam line for transmission measurements of the parent ion beam. The interaction region is pumped by a $3000\,\mathrm{l\,s}^{-1}$ freon baffled oil diffusion pump (effective pumping speed $1000\,\mathrm{l\,s}^{-1}$) providing a residual gas pressure of 5×10^{-8} mbar. Additional liquid-nitrogen-cooled copper plates (8) installed in the vacuum chamber where the beams intersect and in the magnet chambers reduce the pressure during the experiments to 1×10^{-8} mbar along the ion-beam line between the two magnets (7, 15).

2.2. Ion source and transport

The electron-beam ion source and its operation has been described previously. Presently, the highest charge state obtained is $q=15$ for xenon ions with an intensity of 200 ions/s measured behind a collimator made of two apertures each of 0.6 mm diameter 85 mm apart. The energy spread of the ions is less than $30\,q$ eV at an energy of $10\,q$ keV.

Iris apertures (6) are used to adjust the ion-beam intensity to the experimental demands. (The single particle detector is used at count rates not exceeding $10^4\,\mathrm{s}^{-1}$.)

In front of the electron beam the ion beam is collimated by two apertures (0.5 mm diameter, 230 mm apart) resulting in a maximum beam divergence of less than ±0.25°. Thus the diameter of the ion beam inside the electron beam is definitely less than 1.5 mm which could also be proved with the iris aperture (12). When the diameter of this iris aperture is increased beyond 1.5 mm diameter both the parent and product ion intensities measured at (14, 15) and (19), respectively, do not further increase. From this result we conclude that there is 100% transmission of parent and product ions to their detectors. By the iris aperture (17) we could also prove that the ion beams are within a diameter of 5 mm behind the magnet and therefore can completely be collected by the single-particle detector (19) with an effective surface of 20 mm diameter. The height of the magnet chamber is 30 mm.

In general we used isotope 132 of xenon for the present measurements. In the case of Xe^{3+} isotope 129 was employed to avoid possible beam contamination with CO_2^+ ions.

Possible fractions of metastable ions in the incident beams were not directly determined. However, previous measurements employing the electron beam ion source gave no evidence for the production of metastable ions in the ion source, while the population of long-lived excited states in charge transfer collisions *could* be detected. The methods used for these investigations are based on ion–atom collisions in two independent gas cells. Possible reasons for the absence of highly excited metastable ions in our beam have been discussed previously (Müller *et al* 1976a, b, 1980, Seim

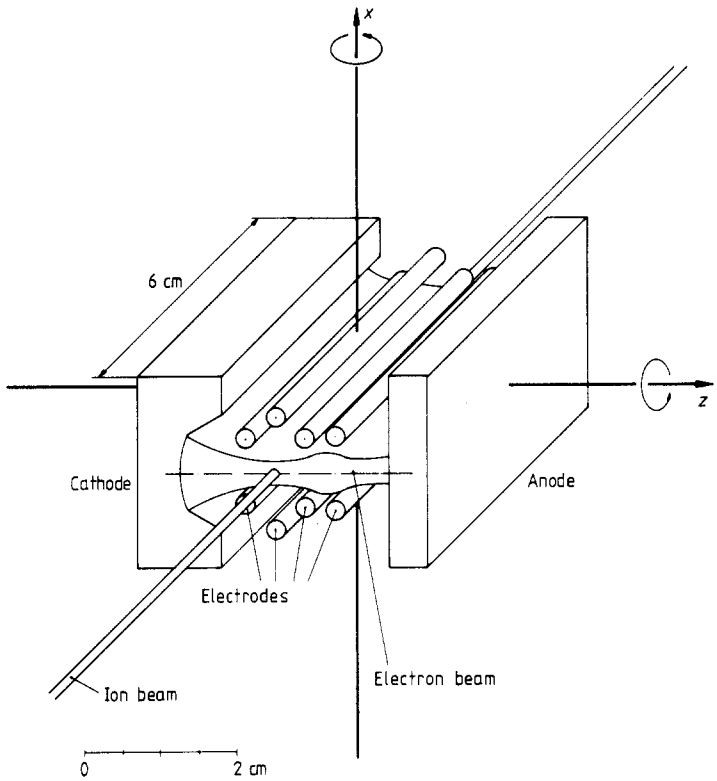

Figure 2. Perspective view of the ion beam crossing the electron beam.

et al 1981). Metastable ions with low excitation energy could probably not be detected by the techniques used, since their cross sections for stripping and charge transfer in ion–atom collisions can be expected to be not much different from those of ground-state ions. If this is the case fractions of ions in low-lying metastable states also would not seriously affect the cross sections to be measured in the present experiment.

2.3. Electron gun

The electron gun previously used by Müller *et al* was modified to provide an improved definition of the electron energy. Instead of three rod electrodes the gun is now equipped with four such electrodes (see figure 2). With the rod potentials shown in figure 3 the potential distribution calculated for the gun by including both the electron space charge and thermal spread of the emitted electrons' energies, exhibits a large symmetrical field-free region where the ion beam crosses the electron beam. The potential at the position of the crossing ion beam is calculated to be 67.5% of the anode potential U_A, when the cathode potential $U_C = 0$. This potential defines the electron energy. It is constant within $\pm 0.3\%$ in an area of $3 \times 3\ \text{mm}^2$ in the xz plane (see figure 3) perpendicular to the ion-beam axis.

The perveance of the present arrangement is between 11 $\mu\text{A V}^{-3/2}$ at $U_A = 30$ V and 8.8 $\mu\text{A V}^{-3/2}$ at $U_A = 1000$ V which means a maximum power of 300 W deposited on the water-cooled copper anode. The change of perveance is due to voltage-dependent influence of the thermal energy spread of electrons emitted from the

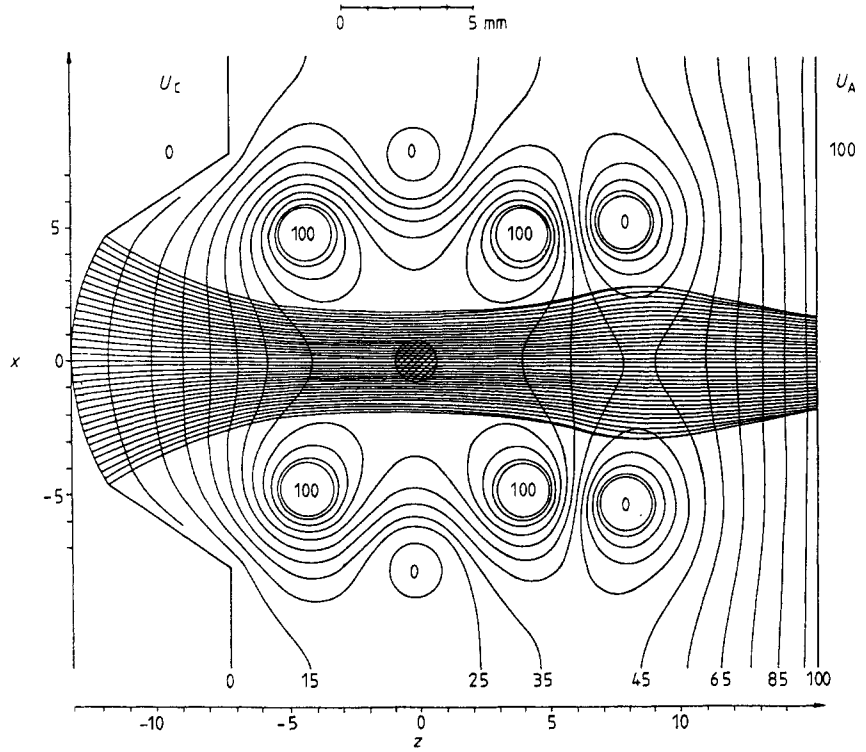

Figure 3. Equipotential lines and electron trajectories of the electron gun calculated in a plane perpendicular to the ion beam. The cross hatched area marks the region of ion penetration. The electric potentials applied to the different electrodes are given in per cent of the voltage U_{CA} between cathode and anode.

impregnated tungsten cathode. All electrodes of the gun are insulated from each other and from ground potential so that it is possible to shift the potential of the interaction region of the two beams to any desired value.

The electron gun is mounted on a complex vacuum manipulator which allows the electron beam to be aligned exactly to the ion beam and the electron beam to be moved completely out of the ion-beam line without breaking the vacuum. Since the electron beam is 6 cm wide in the ion-beam direction a rotation of the electron gun around an axis along the central electron trajectory (axis z in figure 2) was provided to align the ion beam and the electron-beam ribbon. A second rotation is possible around an axis perpendicular to the electron and ion beams (axis x in figure 2) to keep the cathode and anode blocks parallel to the ion beam. Additionally the gun can be moved in the direction of the electron beam and perpendicular to both beams ($\pm z$ and $\pm x$ direction, see figure 2) to allow the adjustment of the ion-beam centre in the plane shown in figure 3.

An accurate alignment of the gun is necessary to keep the ion beam in a region of defined potential. This experimental condition is due to the special requirements realised with the present arrangement: a high density electron beam with a defined electron energy in the region where the ion beam crosses. The present gun provides such an electron beam which even has a uniform current density where the ion beam intersects. It is thus possible to obtain extremely high signal-to-background ratios r for ionisation experiments ($r = 160$ could be obtained).

2.4. Ion detection

The product ions are detected by a single-particle detector with an effective surface of 20 mm diameter and uniform efficiency of (95 ± 3) % for ions with energies above 5 keV. Operation and properties of the detector were described in detail by Rinn *et al* (1982).

The parent ions are collected by a 25 cm long Faraday cup 2 cm high and 1.5 cm deep. Secondary electrons are suppressed by a voltage of −150 V applied to a repeller electrode in front of the ion collecting surface. The cup is installed inside the magnet chamber and allows parent ion currents to be measured simultaneously with the product ions for different charge ratios $q_{\text{parent}}/q_{\text{product}}$ without moving the cup and breaking the vacuum.

3. Cross section measurement

For 90° crossed beams, cross sections are determined from

$$\sigma(E) = \frac{R}{I_e I_i} \frac{qe^2 v_i v_e}{(v_e^2 + v_i^2)^{1/2}} F \tag{1}$$

where $\sigma(E)$ is the absolute cross section at energy E, R is the rate of product ions, I_e and I_i are the electron- and ion-beam currents, q is the charge state of the ions, e the charge of an electron, v_e and v_i are the electron and ion velocities and F is the form factor describing the beam overlap.

In the present experiment the electron-beam current density $j_e(E)$ is constant over the whole interaction region of the two beams so that the form factor becomes

$$F = \frac{I_e}{j_e b_e} \tag{2}$$

where b_e is the electron-beam width passed by the ions ($b_e = 60$ mm). For separating the signal R from background B the rate of ionised ions produced between the two magnets was measured with the electron beam aligned to the ion beam ($R + B$) and then with the operating electron gun moved out of the ion-beam line without switching off the electron beam (B). By this procedure additional background produced by the intense electron beam is correctly taken into account.

In the following subsections the experimental procedure will be discussed in detail, possible sources of error like ion trapping are carefully investigated.

3.1. Electron-beam current density

The electrode arrangement of the electron gun is optimised with respect to uniform potential and constant electron current density j_e in the region where the ion beam crosses. We made two experimental tests to verify constant j_e.

(i) A narrow Ar^+ beam with a diameter less than 0.8 mm was passed through the electron beam and the ionised ions Ar^{2+} were detected for different electron energies. By moving the operating electron gun and observing the Ar^{2+} signal the region of constant electron current density can be found: the Ar^{2+} signal remained constant as long as the electron gun was moved not more than ±1.5 mm perpendicular to both beams and not more than ±2 mm in electron beam direction. Constant ionisation signal indicates constant electron current density within those limits.

(ii) The diameter of the ion beam was increased from 0.8 mm up to 3.5 mm by using different apertures (9, 10 in figure 1) mounted on rotatable wheels which can be operated from outside the vacuum. The ratio R/I_i of signal and incident ion current remained constant within ±3% as long as only the ion-beam diameter was changed to values below 3 mm. This is only possible if the form factor F and hence the electron current density remain constant. (The width of the electron beam is $b_e = 60$ mm according to the length of the cathode block).

The determination of the form factor F is complicated in the present experiment due to the sophisticated electron gun design. Scanning the beams with a metal slit might influence the potential distribution and hence also change the electron current density distribution. We decided therefore to make a relative measurement of F by normalisation of apparent cross sections $\sigma_{1,2}$ for Ar^+ ions to absolute data obtained by Woodruff *et al* (1978). Woodruff *et al* claimed high accuracy (absolute uncertainty less than 10%) for their cross sections, Ar^+ ions are easy to obtain and the threshold electron energy is comparatively low. Our measurements of the normalised electron current density $j_e b_e/I_e$ are shown in figure 4 as a function of the voltage U_{CA} between cathode and anode. The data points exhibit a linear dependence in the semi-logarithmic plot which can be expressed in the form

$$1/F = j_e b_e/I_e = [(-0.48\pm0.05) + (1.26\pm0.02)\ \lg U_{CA}/V] \qquad (\mathrm{cm}^{-1}). \tag{3}$$

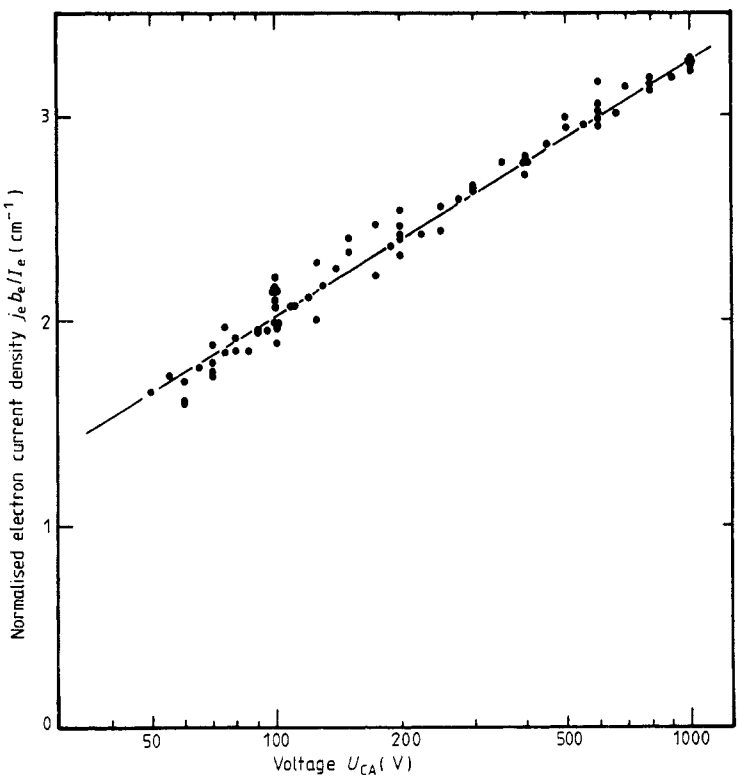

Figure 4. The measured normalised electron current density $j_e b_e/I_e$ in the region of the crossing ion beam. The straight line is the best fit through the data points (see text, equation (3)). The statistical error of the data points is smaller than the size of the points.

Such a linear dependence was also predicted by numerical calculations of Sinz (1981) for electron guns including thermal effects. The scatter in the data is not due to counting statistics; it rather shows the reproducibility of a single cross section measurement for Ar^+ ions. The resulting relative uncertainty in the determination of the form factor F depends on U_{CA} and is normally about ±4%; it does not exceed ±6%. In addition, a systematic error of F may arise from the uncertainty of the data used for normalisation.

3.2. Signal and background

For the measurement of ionisation cross sections the region of the interacting beams was kept at ground potential to avoid lens effects on the transmitted ion beam. Signal and background were measured with the electron beam aligned to the ion beam and background was determined by moving the electron gun out of the ion-beam line without switching off the electron beam. By this procedure background due to gas desorption from the anode by the electron beam can be ruled out when the residual gas pressure in the ion-beam line does not change with the moving electron gun (there is no effect of the electron beam itself on the ion detector 19 in figure 1). This condition was checked by employing an electron capture reaction: a beam of Ne^{4+} ions was used to probe the gas pressure within and outside the electron beam by charge transfer reactions leading to Ne^{3+}. The signal of Ne^{3+} ions increased with increasing electron energy, however, it was the same for the two positions of the electron gun within ±5%. for different ratios of signal R and background B the relative uncertainty of the signal due to an error ΔB in the determination of the background is given by

$$\Delta R/R = \Delta B/R \leqslant 0.05\, B/R. \tag{4}$$

The dependence of R/B on electron energy E has been discussed by Müller *et al* (1980) who showed that R/B increases with E. At high electron energies with R/B of order ten the error ΔB becomes negligible. At values of $R/B < 1$ $\Delta R/R$ rises above 5%. $R/B < 1$ is found only near the threshold of the ionisation process to be investigated. In our experiment we had $R/B > 1$ for electron energies $E \geqslant E_a$ with $E_a = 22$ eV for the ionisation of Xe^+ ions (threshold energy $I_{1,2} = 21.2$ eV) with

$E_a = 40$ eV for Xe^{2+} ions (threshold energy $I_{2,3} = 32.1$ eV),

$E_a = 50$ eV for Xe^{3+} ions (threshold energy $I_{3,4} = 43$ eV) and

$E_a = 90$ eV for Xe^{4+} ions (threshold energy $I_{4,5} = 55$ eV).

Hence an increased uncertainty in the measured cross section is only present in the nearest threshold region. There is one additional source of background which cannot be handled by the procedure discussed. In any electron–ion beams experiment the electron beam produces an additional target of slow residual gas ions for the incident ion beam. The rate of slow ions produced per unit length in electron-beam direction is

$$\dot{N}/d = \sigma_i p/(kT) I_e/e \tag{5}$$

where p is the residual gas pressure, k is Boltzmann's constant, T the absolute gas temperature and σ_i the ionisation cross section for residual gas atoms. For an estimate of $\dot{N}$ we use the maximum diameter of the ion beam $d = 1.5$ mm, the maximum pressure $p = 3 \times 10^{-8}$ mbar ever measured during the experiments and the maximum electron

current $I_e = 300$ mA. With an estimated $\sigma_i = 10^{-16}$ cm^2 the rate of slow ions produced in the volume occupied by the incident ion beam is $\dot{N} = 4 \times 10^{10}$ s^{-1}. When these ions drift out of the interaction region with thermal velocity along the incident ion-beam direction their containment time is less than $\tau = 10^{-4}$ s resulting in a density of the additional slow-ion target $n_i = 4\tau\dot{N}/(\pi d^2 b_e) < 8 \times 10^6$ cm^{-3}. This density is about 100 times less than the electron density and can be neglected. If, however, ion trapping would occur inside the interaction region, n_i might be higher. The calculations of the electron gun which include the electron space charge showed a variation of the electric potential in the interaction region of at most $\Delta U = 0.004 U_{CA}$ forming a radial trap along the fast ion beam. The ends of this trap at the entrance and exit of the ion beam are 'open', slow ions can drift out of this region as assumed in the above estimate of n_i. If the trap were closed by an electrical potential wall the density of the trapped slow ions could be easily calculated under the assumption of a cylindrical symmetric homogeneous distribution of slow ions along the fast ion beam. By integrating the Maxwell equation $\nabla \cdot (\nabla U) = n_i e/\varepsilon_0$ for the column of slow ions with density n_i, which fill the radial trap with a radius of 2 mm and a depth ΔU we obtain with the dielectric constant $\varepsilon_0 = 8.85 \times 10^{-12}$ F m^{-1}

$$n_i = \frac{4\varepsilon_0 \Delta U}{e r_1^2} = 2.2 \times 10^5 \, (U_{CA}/V) \text{ cm}^{-3}. \tag{6}$$

The rate of fast ions which would be ionised by collisions with these slow ions is

$$S = \sigma_{str} n_i b_e I_i/(qe) \tag{7}$$

with σ_{str} representing the ionisation cross section of the ion–ion collision. On the other hand the rate of fast ions ionised by electron impact is approximately given by (see equations (1) and (2))

$$R = \sigma_{q,q+1} j_e b_e I_i/(qe^2 v_i). \tag{8}$$

The ratio of signal R to additional background S is given by

$$z = R/S = \sigma_{q,q+1} j_e/(\sigma_{str} n_i v_i e). \tag{9}$$

With $j_e b_e/I_e$ from equation (3), $I_e \simeq 10^{-5} A U_{CA}^{3/2} V^{-3/2}$ and n_i from equation (6) we find

$$z = \sigma_{q,q+1}/\sigma_{str} \frac{1}{v_i} \frac{(a + b \lg U_{CA}/V) \, (\text{cm}^{-1}) \, 10^{-5} A U_{CA}^{3/2} V^{-3/2}}{b_e (2.2 \times 10^5) U_{CA} V^{-1} (\text{cm}^{-3}) (1.6 \times 10^{-19}) As}. \tag{10}$$

The ratio z becomes smallest at the threshold of $\sigma_{q,q+1}$. With the assumption of $\sigma_{str} = 10^{-17}$ cm^2 at the low centre of mass energies involved for Xe ions incident on the dominant residual gas component H_2O^+, z is greater than 100 at $E_e \simeq 22$ eV for Xe^+, at $E_e \simeq 33$ eV for Xe^{2+}, at $E_e \simeq 45$ eV for Xe^{3+} and at $E_e \simeq 62$ eV for Xe^{4+}.

Thus it is again only in the closest vicinity of the ionisation threshold that considerable errors in the cross section measurements due to an additional slow-ion target may occur.

We mention three test measurements made to assure correct determination of cross sections:

(i) The electron gun operates in the space-charge limited mode; an increase in cathode temperature may not change the electron current. For temperatures between 700 and 1000 °C the electron current was found to be constant within ±1%. The working temperature was always 850 °C;

(ii) The measured ionisation cross sections may not depend on the ion energy. This was checked and proved for ion energies between $4q$ keV and $16q$ keV;

(iii) The measured ionisation cross sections may not depend on the ion current. Measurements were made with I_i between 1 pA and 1 nA for single ionisation of Ne^+ and Xe^+ resulting always in the same cross section within the usual reproducibility.

3.3. Experimental uncertainties

In table 1 typical experimental data are listed for the measurement of electron impact ionisation of Xe^+ and Xe^{4+} ions at two different electron energies. For the determination of signal and background the electron gun was moved up to eight times between the two positions 'in' the ion beam and 'out' of the ion beam. By the high ionisation efficiency of the electron beam it was no problem to limit the statistical counting error (95% confidence level) below 1%. Only within a few eV above the ionisation threshold the statistical error could reach several per cent but was always less than the uncertainty of the background determination.

In table 2 the experimental uncertainties for the cross section measurements and the electron energy are listed. The main sources of error have been discussed already above. The quadrature sum of all individual relative errors gives the typical total uncertainty for electron energies $E \geqslant E_a$, where E_a is the electron energy at which the ratio of signal and background R/B becomes greater than one (see § 3.2).

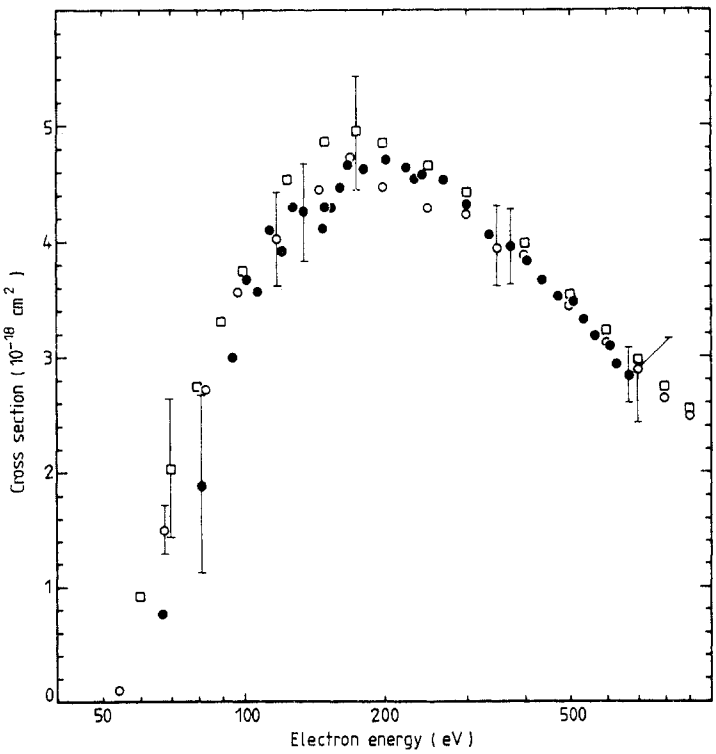

Figure 5. Comparison of measured ionisation cross sections for He^+ ions (●), with data of Dolder *et al* (1961) (□), and Peart *et al* (1969) (○).

Table 1. Typical experimental data for single ionisation of Xe^{+} and Xe^{4+}. Residual gas pressure: 1 to 3×10^{-8} mbar; collimating apertures, first aperture: 0.5 mm; second aperture: 0.6, 0.7 mm.

Reaction	Electron energy E_e(eV)	Ion current I_i(nA)	B/I_i ($s^{-1}\,nA^{-1}$)	Signal R ($10^3\,s^{-1}$)	Background B ($10^3\,s^{-1}$)	R/B
$e+Xe^{+}\rightarrow Xe^{2+}+2e$	40	0.3	400	1.8	0.1	18
	600	0.03	800	3	0.02	150
$e+Xe^{4+}\rightarrow Xe^{5+}+2e$	100	0.3	600	0.5	0.2	2.5
	600			3.5	0.2	17.5

Table 2. Experimental uncertainties.

Source	Uncertainty (%)
Cross section $\sigma_{q,q+1}$	
Counting statistics (typical value above ionisation threshold at 95% confidence level)	±1
Uncertainty in background determination	
$\Delta B/R$ (see equation (4)) for $E \geqslant E_a$	$<\pm 5\%$
Form factor F (relative uncertainty of $j_e b_e/I_e$ from figure 4)	±4
Additional systematic uncertainties	
Counting efficiency	±3
I_i	±2
I_e	±2
v_i	±1
Absolute uncertainty of F due to normalisation to data of Woodruff *et al*	±4 to ±15
Quadrature sum (typical total uncertainty)	±9.2 to ±11.9
Electron energy E	
Measurement of the potential U_{CA}	±3
Uncertainty of calculated electron energy (estimate)	±0.2

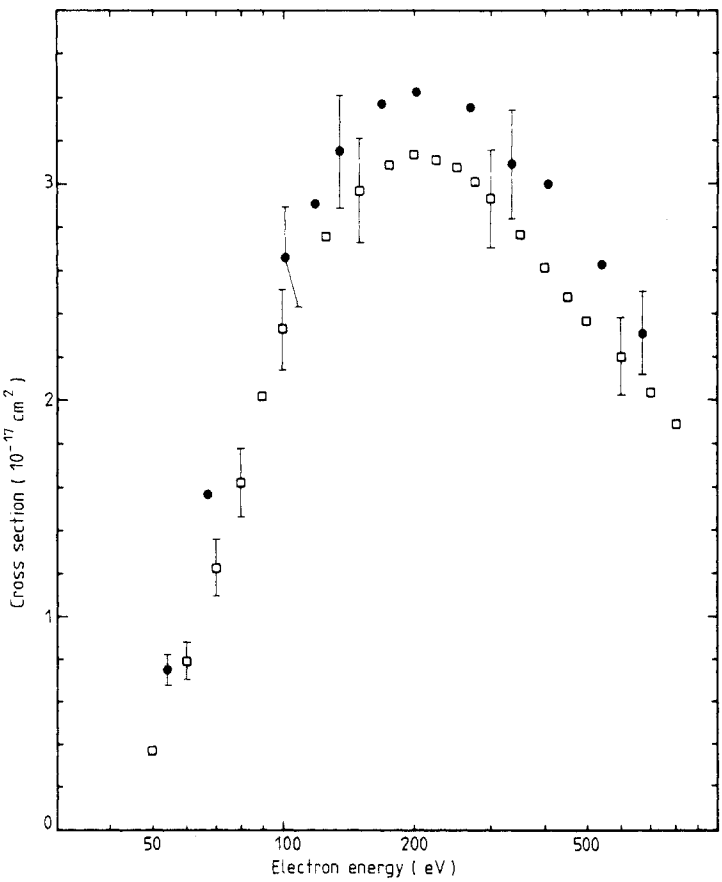

Figure 6. Comparison of measured ionisation cross sections for Ne^+ ions (●), with data of Dolder *et al* (1963) (□).

The electron current density j_e is determined in this experiment by a normalisation to ionisation cross sections $\sigma_{1,2}$ for Ar^+ ions measured by Woodruff *et al* (1978). Hence, the present results automatically agree with their data. With j_e calibrated in this way we also remeasured ionisation cross sections for He^+ and Ne^+ ions (see figures 5 and 6). Our results for He^+ agree with previous measurements for He^+ obtained by Dolder *et al* (1961) and Peart *et al* (1969). These measurements have been confirmed by Defrance *et al* (1981) at lower energies and also agree with the best theoretical calculations presently available (Rudge and Schwartz 1966, Younger 1980). With the same normalisation as before we find a slightly higher cross section $\sigma_{1,2}$ for Ne^+ ions than Dolder *et al* (1963), the discrepancy, however, is well within the error bars of both experiments. The cross sections measured by the method described here are generally about 20% greater than those obtained by Müller *et al* (1980) who used a different way to determine j_e. On the other hand data for Ar^{3+} and Ar^{4+} previously measured by Müller *et al* (1980) are in reasonable agreement with experimental data of the Oak Ridge group (Gregory *et al* 1983, Crandall 1982b) while the present normalised measurements for Xe^{3+} ions are about 20% above the data of Gregory *et al* (1983) (which is again within the combined uncertainties of both experiments).

4. Results and discussion

We have measured electron impact ionisation cross sections $\sigma_{q,q+1}$ for

$$e + Xe^{q+} \rightarrow Xe^{(q+1)+} + 2e \qquad q = 1, 2, 3, 4.$$

The data are compiled in table 3 together with estimates of the overall error (see § 3.3). For the estimate of the possible error of the form factor F the relative uncertainty of $j_e b_e / I_e$ from figure 4 and—throughout the whole energy range—an absolute uncertainty of ±9% due to the normalisation were considered, although some cross section values of Woodruff *et al* used for the normalisation have an overall uncertainty of more than 15%. However, since we take into account the course of the whole cross section function for the form factor evaluation, the use of an averaged uncertainty of the results of Woodruff *et al* appears to be reasonable.

Table 3. Electron impact ionisation cross sections $\sigma_{q,q+1}$ of Xe^{q+} ions ($q = 1, 2, 3, 4$). Estimated *overall* uncertainties are given. The cross section data are displayed in general with three digits because relative uncertainties are much less than the total error.

Electron energy (eV)	Cross section (10^{-17} cm^2)	Electron energy (eV)	Cross section (10^{-17} cm^2)
$\sigma_{1,2}$ $Xe^+ \rightarrow Xe^{2+}$			
16.9	0.9±1.0	27.0	18.0±3.0
16.4	0.3±0.9	28.7	20.8±3.1
17.6	0.3±0.9	28.7	21.4±3.2
18.6	0.5±0.8	30.4	22.2±3.2
19.6	0.9±1.0	32.0	24.7±2.9
20.3	1.9±1.1	33.8	24.7±2.8
21.9	6.5±2.1	33.8	24.4±2.7
23.6	11.7±2.7	35.6	25.1±2.8
23.6	10.8±2.5	37.1	24.7±2.7
25.3	15.3±3.0	38.8	25.4±2.7

Table 3. (continued)

Electron energy (eV)	Cross section (10^{-17} cm^2)	Electron energy (eV)	Cross section (10^{-17} cm^2)
40.5	24.6±2.6	148.5	15.8±1.7
42.2	24.7±2.7	151.9	16.1±1.7
43.9	24.1±2.6	162.0	15.3±1.6
45.5	23.6±2.5	168.8	15.5±1.7
47.3	24.0±2.6	175.5	15.0±1.6
48.9	23.3±2.5	185.6	14.7±1.6
50.6	23.7±2.6	189.0	14.4±1.5
50.6	23.9±2.6	202.5	13.8±1.5
52.3	23.2±2.5	202.5	13.9±1.5
55.7	22.9±2.5	219.5	13.4±1.4
59.1	22.7±2.4	236.3	13.0±1.4
60.8	22.6±2.4	253.1	12.3±1.3
64.1	22.3±2.4	270.0	12.4±1.3
67.5	22.7±2.4	270.0	12.0±1.3
67.5	22.2±2.4	290.3	11.4±1.2
70.9	21.9±2.4	310.5	11.1±1.2
74.3	21.5±2.3	337.5	10.2±1.1
81.0	21.0±2.3	337.5	10.6±1.1
81.0	21.9±2.4	371.3	9.88±1.1
84.4	21.1±2.3	405.0	9.30±1.0
87.8	20.3±2.2	405.0	9.20±0.99
94.5	19.5±2.1	438.8	8.79±0.95
101.3	19.4±2.1	472.5	8.18±0.88
101.3	20.2±2.2	506.3	8.08±0.87
108.0	18.8±2.0	540.0	7.60±0.82
108.0	19.5±2.1	540.0	7.63±0.82
114.8	18.8±2.0	573.8	7.26±0.78
118.1	17.9±1.9	607.5	7.04±0.75
121.5	18.1±1.9	641.3	6.80±0.73
135.0	16.9±1.8	675.0	6.50±0.70
135.0	17.0±1.8	675.0	6.34±0.68
$\sigma_{2,3}Xe^{2+} \rightarrow Xe^{3+}$			
20.3	−0.7±3	59.1	14.4±1.8
27.0	2.1±3	60.8	14.5±1.9
27.0	4.3±3	60.8	13.9±1.7
30.4	6.4±6	64.1	14.8±1.9
30.4	8.3±7	67.5	14.2±1.9
30.4	4.8±5	67.5	14.3±1.8
32.1	7.3±6	67.5	14.5±1.8
33.8	11.5±4	67.5	14.4±1.8
33·8	9.2±3	70.9	15.8±1.9
33.8	9.9±3	74.3	14.5±1.7
35.1	11.4±2.3	74·3	15.1±1.8
37.1	10.9±2.2	81.0	14.3±1.7
37.3	12.2±2.1	81.0	14.0±1.6
40.5	12.8±2.2	84.4	15.2±1.8
42.2	14.0±2.2	84.4	14.7±1.7
45.6	14.5±2.2	87.8	14.7±1.7
47.3	13.6±2.0	87.8	14.1±1.6
48.9	14.1±2.1	91.1	15.3±1.8
54.0	14.9±2.2	94.5	13.9±1.7
55.7	14.6±1.9	94.5	13.8±1.6

Table 3. (continued)

Electron energy (eV)	Cross section (10^{-17} cm^2)	Electron energy (eV)	Cross section (10^{-17} cm^2)
101.3	13.6±1.5	283.5	6.75±0.73
101.3	14.6±1.6	303.8	6.31±0.68
101.3	13.7±1.5	303.8	6.17±0.66
101.3	13.3±1.4	320.6	6.24±0.67
108.0	13.1±1.4	337.5	5.82±0.63
114.8	13.0±1.5	337.5	5.99±0.65
118.1	12.0±1.4	354.4	5.73±0.62
121.5	12.0±1.3	371.3	5.58±0.60
135.0	10.7±1.2	371.3	5.47±0.59
135.0	11.3±1.2	388.1	5.30±0.57
148.5	10.5±1.1	405.0	4.98±0.54
162.0	9.91±1.1	405.0	5.23±0.56
168.8	8.72±0.94	405.0	5.57±0.60
175.5	9.50±1.0	425.3	5.05±0.54
189.0	8.73±0.94	445.5	4.81±0.52
202.5	8.09±0.87	465.8	4.66±0.50
202.5	8.02±0.86	486.0	4.46±0.48
202.5	8.24±0.89	506.3	4.29±0.46
216.0	7.96±0.86	533.3	4.16±0.45
229.5	7.67±0.83	540.0	4.13±0.44
236.3	7.21±0.78	560.3	3.99±0.43
243.0	7.49±0.81	587.3	3.80±0.41
270.0	6.89±0.74	614.3	3.61±0.39
270.0	6.76±0.73	641.3	3.49±0.38
270.0	6.76±0.73	675.0	3.57±0.38
		675.0	3.33±0.36
$\sigma_{3,4}Xe^{3+} \rightarrow Xe^{4+}$			
16.9	0.3±3	114.8	9.19±1.5
33.8	0.9±2	128.3	8.04±1.3
37.1	0.3±0.5	135.0	7.05±1.1
40.5	0.8±0.5	141.8	7.34±1.1
40.5	0.5±0.5	155.3	6.62±0.95
43.9	2.4±0.6	168.8	6.01±0.89
43.4	2.4±0.6	182.3	5.57±0.75
47.3	3.66±0.73	195.8	5.34±0.68
47.3	3.26±0.65	202.5	5.31±0.65
50.6	4.06±0.75	216.0	5.09±0.60
50.6	3.66±0.73	229.5	4.97±0.55
54.0	4.57±0.90	243.0	4.87±0.54
54.0	4.05±0.80	256.5	4.70±0.52
57.4	4.97±0.90	270.0	4.76±0.52
60.8	5.80±1.0	283.5	4.52±0.50
64.1	7.25±1.3	297.0	4.42±0.49
67.5	8.46±1.5	310.5	4.45±0.49
67.5	7.84±1.4	324.0	4.36±0.48
67.5	7.28±1.3	337.5	4.02±0.44
74.3	9.33±1.5	354.4	3.97±0.44
81.0	10.4±1.6	371.3	3.83±0.42
87.8	10.9±1.7	391.5	3.71±0.41
94.5	11.2±1.8	411.8	3.70±0.41
101.3	10.6±1.7	438.8	3.59±0.39
108.0	9.89±1.6	465.8	3.49±0.38

Table 3. (continued)

Electron energy (eV)	Cross section (10^{-17} cm^2)	Electron energy (eV)	Cross section (10^{-17} cm^2)
499.5	3.33±0.37	567.0	3.08±0.35
533.3	3.17±0.35	607.5	2.90±0.32
		641.3	2.82±0.31
		675.0	2.73±0.30
$\sigma_{4,5}Xe^{4+} \rightarrow Xe^{5+}$			
40.5	0.7±1		
43.9	0.7±1	172.1	5.68±0.80
47.3	0.8±1	182.3	5.45±0.76
47.3	0.5±1	185.6	5.76±0.78
50.6	0.9±1	195.8	5.26±0.71
50.6	0.9±1	202.5	5.38±0.73
54.0	0.0±1	202.5	5.41±0.73
54.0		205.9	5.23±0.71
57.4	4.4±1	216.0	5.13±0.69
57.4	3.9±1	219.4	5.45±0.74
60.8	5.0±1	229.5	5.12±0.69
60.8	4.7±1	236.3	5.14±0.69
60.8	4.5±1	236.2	4.85±0.65
64.1	6.15±1.2	243.0	4.99±0.67
67.5	6.02±1.1	256.5	4.95±0.67
67.5	6.47±1.2	270.0	4.83±0.65
67.5	6.11±1.1	270.0	5.02±0.68
67.5	6.21±1.1	270.0	4.94±0.67
67.5	6.35±1.2	283.5	4.75±0.64
70.9	7.88±1.5	297.0	4.73±0.64
74.3	7.84±1.5	303.8	5.12±0.69
77.6	8.50±1.6	310.5	4.61±0.62
77.6	8.75±1.6	324.0	4.49±0.61
84.4	8.95±1.6	337.5	4.41±0.60
91.1	8.97±1.6	337.5	4.53±0.61
94.5	8.04±1.3	354.4	4.48±0.59
97.9	8.85±1.5	371.3	4.39±0.57
101.3	8.33±1.3	391.5	4.32±0.56
101.3	7.66±1.2	411.8	4.25±0.55
104.6	8.18±1.3	425.3	4.20±0.54
108.0	7.75±1.2	445.5	4.12±0.53
111.4	7.72±1.2	465.8	4.09±0.52
114.0	7.70±1.2	486.0	4.09±0.52
118.1	7.76±1.2	506.3	3.98±0.51
118.1	7.89±1.2	526.5	3.93±0.50
121.5	7.76±1.2	546.8	4.00±0.51
121.5	7.26±1.1	567.0	3.88±0.49
124.9	7.47±1.1	587.3	3.72±0.47
131.6	7.14±1.0	607.5	3.80±0.48
135.0	6.81±0.95	607.5	3.75±0.47
141.8	6.71±0.94	607.5	3.86±0.48
148.5	6.38±0.89	607.5	3.82±0.48
151.9	6.51±0.91	607.5	3.81±0.48
151.9	6.27±0.88	624.4	3.70±0.47
162.0	6.00±0.84	641.3	3.67±0.46
168.8	5.84±0.82	658.1	3.50±0.47
168.8	5.76±0.81	675.0	3.75±0.42
		675.0	3.46±0.42

As discussed in the previous section, considerable total uncertainties of cross section measurements are obtained in the threshold region by the present experimental technique. For all data sets $\sigma_{q,q+1}$ ($q = 1, 2, 3, 4$) we give results of cross section measurements at electron energies of 5 to 25 eV below threshold to show the uncertainty and the scatter of these data.

In the case of $\sigma_{1,2}$ there is only one out of six measured cross sections non-zero below threshold within the range of estimated errors. In general, these values are well below 5% of the cross section maximum. Within these limits there is no definite sign of metastable contamination of the parent Xe^+ beam.

In the case of the $\sigma_{2,3}$ signal below threshold was observed (although uncertainties of these values are of order 100% due to the problems with background determination discussed in § 3.1). A possible parent beam component of Xe^{2+} ions in the lowest metastable states ($5p^4$: $^3P_0$, $^3P_1$, $^1D_2$, $^1S_0$) cannot definitely be ruled out on the basis of the present data.

In the cases of $\sigma_{3,4}$ and $\sigma_{4,5}$ again the cross sections measured below threshold are zero within their overall uncertainty. We emphasise again that it is only the region close to and below the threshold where cross section measurements are difficult in this experiment. As discussed before, the background determination does not cause problems at the high signal-to-background ratios obtained for electron energies $E > E_a$ (see § 3.2). Figure 7 shows the measured cross sections along with distorted wave with exchange (DWX) calculations performed by Younger (1982c) and along with cross sections calculated from the semiempirical Lotz formula (Lotz 1968)

$$\sigma_{q,q+1} = 4.5 \times 10^{-14} (\mathrm{eV})^2\,\mathrm{cm}^2 \sum_k n_k \ln(E/E_k^q)/(EE_k^q) \tag{11}$$

with the number of electrons in the kth subshell n_k and the ionisation potential of the kth subshell of the ion Xe^{q+} E_k^q. For comparison with the experimental data we have summed only over the 5p ($k = 1$) and the 5s ($k = 2$) shells of the Xe^{q+} ions. When employing equation (11) one has to be aware of the fact that single ionisation of an inner shell may be followed by Auger decay leading to a further increase of the charge state. Thus the initial ejection of a single electron may be seen only in the cross sections for multiple ionisation. We have shown in a separate paper (Achenbach *et al* 1983) that single ionisation of the 4d shell of Xe^+ ions already predominantly contributes to the double-ionisation cross sections and therefore limited the summation in equation (11) for Xe^{q+} ions to $k = 1$ and 2. The ionisation potentials E_1^q for the outermost shell are known (Moore 1970). For the 5s shell we used energies calculated by Younger (1982c).

The Lotz formula is known to give a reasonable representation for the direct ejection of one electron from an ion. Younger also calculated only the direct-ionsiation cross section. His DWX approximation is probably the best that can presently be done and certainly gives very reliable results for the direct part of the ionisation cross section. The Lotz formula is close to the DWX calculations and both give a reasonable representation of $\sigma_{1,2}$, indicating that the ionisation of Xe^+ is dominated by direct electron ejection.

The situation becomes completely different with the charge states $q \geq 2$ of the Xe ions investigated. With increasing q the measured cross sections $\sigma_{q,q+1}$ increasingly exceed the calculated direct contributions. Especially in the region of $E = 100$ eV the experimental data are up to two times higher for $\sigma_{2,3}$ and up to five times higher for $\sigma_{4,5}$ than the theoretical values. These large discrepancies exhibit the importance of indirect ionisation mechanisms such as excitation–autoionisation processes. The inclusion of these contributions in calculations for the ionisation of Xe^{6+} ions leads to

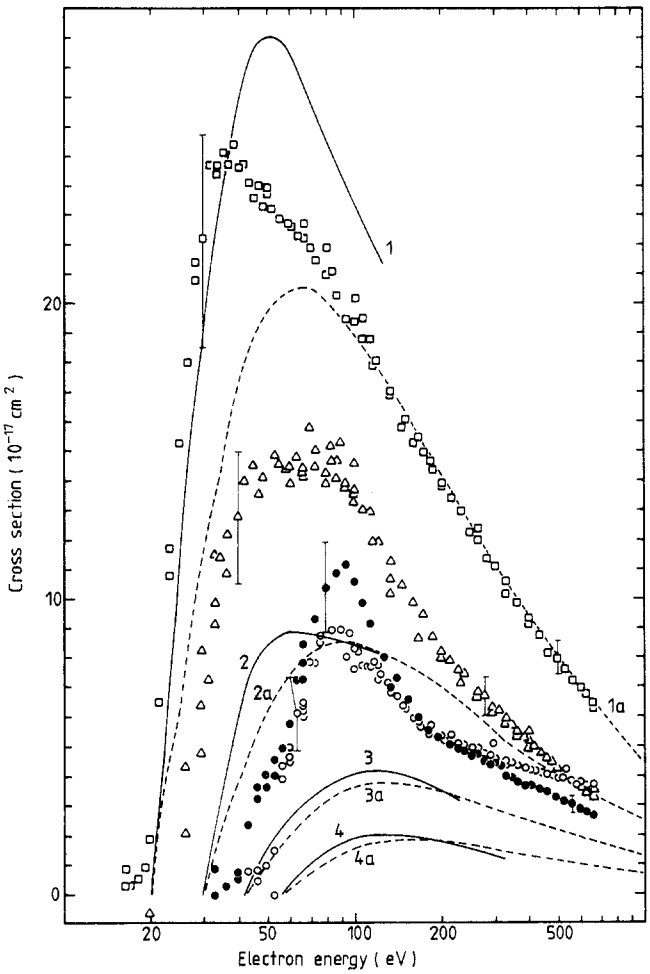

Figure 7. Cross sections for single ionisation of Xe^{q+} ions by electron impact ($\sigma_{q,q+1}$): $e+Xe^{q+} \rightarrow Xe^{(q+1)+}+2e$ ($q=1, 2, 3, 4$). $\sigma_{1,2}$, □, 1, 1a; $\sigma_{2,3}$, △, 2, 2a; $\sigma_{3,4}$, ●, 3, 3a; $\sigma_{4,5}$, ○, 4, 4a. The symbols denote experimental data, the full curves results from Younger (1982c) (5s+5p) and the broken curves results from Lotz (1968) (5s+5p). The error bars mark the total error given in table 2. (For more details see text.)

a good representation of measured cross sections (Pindzola *et al* 1983, Gregory and Crandall 1983). In addition to the unexpected size of the measured cross sections the data show an unusual energy dependence. Especially the cross sections $\sigma_{3,4}$ and $\sigma_{4,5}$ are enhanced for electron energies above roughly 60 eV, have a prominent maximum near 100 eV (see figure 8) and then decrease rapidly at least with E^{-3} for electron energies up to $E \simeq 200$ eV. This arresting feature was first found by Gregory *et al* (1983) (Crandall *et al* (1982b)) for Xe^{3+} ions. It is less dominant for Xe^{4+} ions and only spurious for Xe^{2+} ions. There is another novel feature in our results. For the first time we found a case where $\sigma_{q,q+1}$ increases with increasing q for a fixed ion species: the cross section $\sigma_{4,5}$ is greater than $\sigma_{3,4}$ for energies $E > 200$ eV and even becomes equal to $\sigma_{2,3}$ at about 500 eV. This is in contrast to all theoretical expectations at least for direct ionsiation where $\sigma_{q+1,q+2} < \sigma_{q,q+1}$ is found at fixed electron energy and indicates again the increasing importance of indirect ionisation mechanisms.

Figure 8 also shows a comparison with the data $\sigma_{3,4}$ of Gregory *et al* (1983) which are represented by the full curve. Both measurements find the same shape of $\sigma_{3,4}$ and there is only a minor difference in absolute size which was discussed at the beginning of this section. Gregory *et al* (1983) have already discussed the surprising feature found with $\sigma_{3,4}$ which resembles photoionisation data for the 4d shell of Xe. The onsets of the observed bumps in the cross sections are below the ionisation threshold of the 4d shells of the Xe^{q+} ions which indicates that *excitation* of a 4d electron to a bound state (probably a 4f state) with subsequent autoionisation is responsible for the enhancement of the ionisation cross sections. By measurements of multiple ionisation of Xe^{q+} ions we found dominant contributions of ionisation of a 4d electron to *double* ionisation.

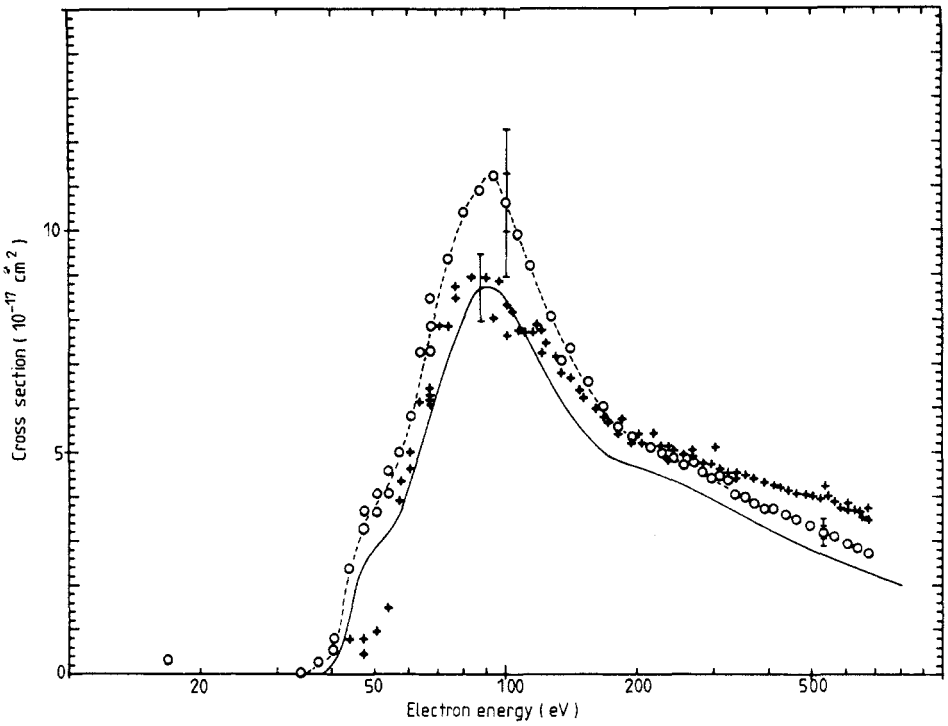

Figure 8. Cross sections for single ionisation of Xe^{3+} ($\sigma_{3,4}$) and Xe^{4+} ($\sigma_{4,5}$) by electron impact. ○, $\sigma_{3,4}$, +, $\sigma_{4,5}$, this work; ——, measurements for $\sigma_{3,4}$ of Gregory *et al.* (The outer error bars for the measurements of this work mark the total error, while the inner error bars mark only the statistical error. The error for the measurements of Gregory *et al* marks the total error.)

The peaked shape of the cross section enhancement in $\sigma_{3,4}$ and $\sigma_{4,5}$ is probably due to term dependent excitation of 4d electrons to 4f states with non-dipole transitions dominating which could explain the E^{-3} energy dependence. Theoretical calculations of Pindzola *et al* (1983) show the influence of term dependence in the Cd-like series which includes Xe^{6+} and which probably can also explain the present results. Calculations are more difficult for charge states lower than Xe^{6+} since then also the spectator electrons in the 5p shell have to be considered.

5. Conclusions

Our measurements show that ionsiation of complex ions can no longer be treated with simple generalisations like the Lotz formula. It is not only the increasing importance of non-direct ionisation mechanisms that makes cross sections difficult to predict but also the necessity to consider correlation effects, complicated couplings of electronic states and the sensitivity of wavefunctions of different terms to the effective core potentials.

Complex ions also have very high cross sections for multiple ionisation. By the measurement of such data additional information can be obtained about the contributions of inner shells e.g. the 4d shell to single and multiple ionisation processes.

In a subsequent paper we shall present cross sections for multiple ionisation processes of multiply charged Xe ions.

Acknowledgments

The authors would like to thank Dr S M Younger for communicating his DWX calculations of the ionisation cross sections prior to publication and his helpful comments. This work was supported in part by the Deutsche Forschungsgemeinschaft.

References

Achenbach C, Müller A, Salzborn E and Becker R 1983 *Phys. Rev. Lett.* **50** 2070–3
Bottcher C, Griffin D C and Pindzola M S 1983 *J. Phys. B: At. Mol. Phys.* **16** L65–70
Crandall D H 1982a *Nato Advanced Study Summer Institute at Cargese, Corsica, France, June 1982* ORNL/TM-8453
—— 1982b *Proc. 12th Int. Conf. on Physics of Electronic and Atomic Collisions, Gatlinburg* ed S Datz (Amsterdam: North-Holland) Invited papers pp 595–608
Crandall D H, Phaneuf R A, Hasselquist B E and Gregory D C 1979 *J. Phys. B: At. Mol. Phys.* **12** L249–56
Defrance P, Brouillard F, Claeys W and van Wassenhove G 1981 *J. Phys. B: At. Mol. Phys.* **14** 103–10
Dolder K T, Harrison M F A and Thonemann P C 1961 *Proc. R. Soc.* A **264** 367–78
—— 1963 *Proc. R. Soc.* A **274** 546–51
Falk R A, Dunn G H, Gregory D C and Crandall D H 1983 *Phys. Rev.* A **27** 762–70
Falk R A, Dunn G H, Griffin D C, Bottcher C, Gregory D C, Crandall D H and Pindzola M S 1981 *Phys. Rev. Lett.* **47** 494–7
Golden L B and Sampson D H 1977 *J. Phys. B: At. Mol. Phys.* **10** 2229–37
—— 1978 *J. Phys. B: At. Mol. Phys.* **11** 3235–43
—— 1980 *J. Phys. B: At. Mol. Phys.* **13** 2645–52
Gregory D C and Crandall D H 1983 *Phys. Rev.* A **27** 2338–41
Gregory D C, Dittner P F and Crandall D H 1983 *Phys. Rev.* A **27** 724–36
Henry R W and Msezane A 1982 *Phys. Rev.* A **26** 2545–50
LaGattuta K J and Hahn Y 1981 *Phys. Rev.* A **24** 2273–6
Lotz W 1968 *Z. Phys.* **216** 241–7
Moore C E 1970 *NSRDS-NBS 34* (Washington, DC: US National Bureau of Standards)
Moores D L 1978 *J. Phys. B: At. Mol. Phys.* **11** L403–5
Moores D L and Nussbaumer H 1969 *J. Phys. B: At. Mol. Phys.* **3** 161–72
Müller A, Klinger H and Salzborn E 1976a *J. Phys. B: At. Mol. Phys.* **9** 291–3
—— 1976b *Nucl. Instrum. Meth.* **140** 181–8
Müller A, Salzborn E, Frodl R, Becker R, Klein H and Winter H 1980 *J. Phys. B: At. Mol. Phys.* **13** 1877–99
Peart B and Dolder K 1975 *J. Phys. B: At. Mol. Phys.* **8** 56–62
Peart B, Walton S and Dolder K T 1969 *J. Phys. B: At. Mol. Phys.* **2** 1347–52

Pindzola M S, Griffin D C and Bottcher C 1983 *Phys. Rev.* A **27** 2331–7
Rinn K, Müller A, Eichenauer H and Salzborn E 1982 *Rev. Sci. Instrum.* **53** 829–37
Rudge M R H and Schwartz S B 1966 *Proc. Phys. Soc.* **88** 563–78
Seim W, Müller A and Salzborn E 1981 *Z. Phys.* A **301** 11–6
Sinz W 1981 *Nucl. Instrum. Meth.* **187** 259–62
Woodruff P R, Hublet M C and Harrison M F A 1978 *J. Phys. B: At. Mol. Phys.* **11** L305–8
Younger S M 1980 *Phys. Rev.* A **22** 111–7
—— 1981 *Phys. Rev.* A **23** 1138–46
—— 1982a *Phys. Rev.* A **26** 3177–86
—— 1982b *Phys. Rev.* A **25** 3396–8
—— 1982c private communication